



3D nanometrology of transparent objects by phase calibration of a basic bright-field microscope for multiple illumination apertures

D. MIGLIOZZI,¹  B. ZHAO,^{1,2} AND M. A. M. GIJS^{1,*}

¹Laboratory of Microsystems, Ecole Polytechnique Federale de Lausanne, Switzerland

²Karlsruhe Institute of Technology, Germany

*martin.gijs@epfl.ch

Abstract: Optical retrieval of the structure of transparent objects at the nanoscale requires adapted techniques capable of probing their interaction with light. Here, we considered a method based on calibration of the defocusing with partially coherent illumination and explored its phase retrieval capability over a wide range of illumination angles. We imaged: (1) commercial dielectric nanospheres to assess the phase calibration when measured along the optical axis, (2) custom-made nano-steps micropatterned in a glass substrate to assess the phase calibration when measured along the transversal axis, and (3) human cancer cells deposited on a glass substrate to assess the results of the calibration on complex transparent 3-dimensional samples. We first verified the model prediction in the spatial frequency domain and subsequently obtained a consistent and linear phase-calibration for illumination numerical apertures ranging from 0.1 to 0.5. Finally, we studied the dependence of the phase retrieval of a complex nanostructured object on the illumination aperture.

© 2020 Optical Society of America under the terms of the [OSA Open Access Publishing Agreement](#)

1. Introduction

Due to the negligible decrease in intensity for the light passing through transparent samples, it may be hard with a basic microscope to quantify the 3D topography of such samples at the nanoscale. On the other hand, scattering events depend on the content and the structure of the interacting object. The phenomenon of light scattering has been used in the past to obtain images of transparent samples by calculating the phase shift induced by the sample on the illumination light. This phase shift is linked to the refractive index of the samples, which, in turn, is a consequence of its composition and structure. Several microscopy techniques were developed to enable such an imaging modality for very complex 3D nanostructured samples such as cells and tissues. Optical coherence was used to distinguish between cancer and normal cells [1]. Partially coherent light with programmable spatial distribution was used to reconstruct the 3-dimensional refractive index of embryos [2]. Phase-shifting laser interferometry with variable illumination angle enabled the 3D mapping of the refractive index of tumor cells and nematode specimens [3], and red blood cells [4]. Holographic detection with sequential illumination angles was combined with complex deconvolution to obtain phase images of bacteria and neuron dynamics [5]. White-light diffraction tomography with spatial light interference was used to retrieve the phase of bacteria and red blood cells [6]. Differential interference contrast imaging combined with transport-of-intensity equation enabled 3D reconstruction of cheek cells and macrophages [7]. Annular illumination combined with the transport-of-intensity equation was used to increase the spatial resolution in subcellular structure imaging [8].

The majority of mentioned techniques require adaptations for the illumination and/or the detection that are not directly implementable on common existing microscopes, which prevents the users of standard bright-field microscopes from benefitting from such technical advances. A simple method that is applicable to standard transmission microscopes without any additional

modification employs the already mentioned transport-of-intensity equation to calculate the information about the 3D phase of the sample by simply using defocused images close to the best-focus plane [8–11]. This method is implementable on standard transmission microscopes, but it is based on the paraxial approximation of the Helmholtz equation, which can limit its applicability. Instead, a model to calculate the transfer function of a simple bright-field microscope using partially-coherent illumination on weakly-scattering objects has been proposed and used for quantitative phase retrieval [6,10,12,13]. It does not use approximations for the Helmholtz equation and is based on the definition of the scattering potential of the object $F(\mathbf{r}) = k_0^2 (n^2(\mathbf{r}) - \bar{n}^2)$ in 3D space (coordinate indicated by \mathbf{r}), which relates to the difference between the refractive index of the object (n) and the one of the surrounding medium (\bar{n}) for a light with wave-vector size k_0 . For non-dispersive objects (*i.e.* n is wavelength-independent) under Koehler illumination (as in standard bright-field transmission microscopes), it was shown that, in the Fourier domain of spatial frequencies \mathbf{g} , a linear relation holds between the scattering potential and the cross-spectral density of the illumination and scattered field:

$$\widehat{\Gamma}(\mathbf{g}) = i\widehat{F}(\mathbf{g})H(\mathbf{g}) \quad (1)$$

$H(\mathbf{g})$ being the modulation transfer function of the system calculated as

$$\int \frac{S(\omega)}{k_{d,z}} \delta(\mathbf{g} - \mathbf{k}_d + \mathbf{k}_i) d\mathbf{k}_i d\mathbf{k}_d d\omega \quad (2)$$

where $S(\omega)$ is the illumination spectrum, \mathbf{k}_i and \mathbf{k}_d are the propagation vectors of the illumination and the scattered fields, respectively, $\delta(\cdot)$ is the Dirac delta function, and the integral is taken over all the possible illumination frequencies and propagation vectors. The shape of such a transfer function along with its dependence on the parameters of the optical microscope is depicted in Fig. 1(a). Previous methods used this approach with the Wiener deconvolution algorithm to retrieve the local refractive index [14]. Another work used a sparse deconvolution algorithm to calculate the local phase [6]. Other work [13] argued that a correction in the retrieval of the quantitative phase should be made in order to account for the specific filtering properties of the optical system: the phase retrieval was performed by recording a stack of bright-field images at low numerical aperture followed by applying some computational steps:

1. Fourier-transformation of the intensity stack $I(\mathbf{r}) \xrightarrow{\mathcal{F}} \widehat{I}(\mathbf{g})$.
2. Filtering by combining the analytical shape of $H(\mathbf{g})$ and a cut-off filter $K(g_z)$ to recover the part of the cross-spectral density $\widehat{\Gamma}_+(\mathbf{g}) = \widehat{I}(\mathbf{g})K(g_z)$ that includes only the spatial frequencies contained in the support of $H(\mathbf{g})$ and excludes the ones in the overlap region (black region in Fig. 1(b)).
3. Inverse Fourier-transformation of the cross-spectral density $\widehat{\Gamma}_+(\mathbf{g}) \xrightarrow{\mathcal{F}^{-1}} \Gamma_+(\mathbf{r})$ and calculation of the calibrated phase

$$\varphi(\mathbf{r}) = \arctan\left(\frac{\alpha \text{Im}(\Gamma_+(\mathbf{r}))}{I_0 + \alpha \text{Re}(\Gamma_+(\mathbf{r}))}\right) \quad (3)$$

where I_0 is the average black intensity and α is a calibration factor that depends on the optical system and its specific spatial filtering properties. This phase is crucially different from the phase commonly retrieved from defocusing in other approaches where a projected phase is calculated (black *e.g.* black with the transport of intensity equations [15] or by 2D differential phase contrast [16]): the phase in Eq. (3) is a truly 3D phase, black *i.e.* black it gives the information of the local phase shift introduced by the sample at any point in

space, accordingly to the spatial frequency content achievable with the transfer function of the optical system. Moreover, the current approach does not require the retrieval of the scattering potential or refractive index, nor any regularization method commonly employed in the corresponding reconstruction algorithms.

This reconstruction algorithm was combined with a custom prism to acquire simultaneous images of different planes of the sample at the same time, enabling to reconstruct the 3D morphology of living samples at high temporal resolution. However, the filtering method and the limited numerical aperture may preclude the access to low and high spatial frequencies. Given the potential benefit of using several illumination apertures when employed for 3D imaging [17,18], here we study the effect of varying the illumination numerical aperture to span a larger region of spatial frequencies and analyse the variation of the calibration factor upon increasing values of the illumination numerical aperture.

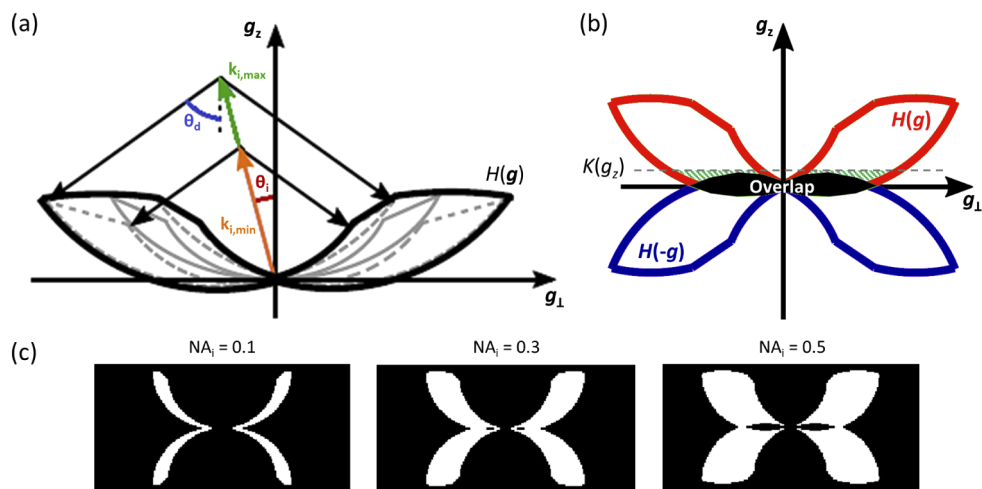


Fig. 1. Transfer function in the Fourier space for several illumination apertures. (a) Schematics of the modulation transfer function $H(\mathbf{g})$ in the Fourier space, and its dependence on the illumination spectrum and on the illumination and detection apertures ($NA_{d,i} = n \sin \theta_{d,i}$). Since $H(\mathbf{g})$ is axysymmetric, only the central cross-section is shown. The grey lines indicate the Ewald's sphere caps for a given pair of illumination (θ_i) and detection (θ_d) angles integrated over the full illumination spectrum (k_i). The black outline indicate the support of $H(\mathbf{g})$ combining all the Ewald's sphere caps. (b) Schematics of the support of the modulation transfer function and its overlapping conjugate. The dashed line indicates the high-pass threshold used in the literature [13] and described in the introduction. The line-patterned area indicates the spatial frequencies gained by using the analytical shape of the modulation transfer function instead of a horizontal cut-off $K(g_z)$ as a threshold. (c) Central cross-section of the support of the modulation transfer function for several illumination apertures.

2. Results

2.1. Modulation transfer function of the transmission microscope

We first show that the cross-spectral density and its complex conjugate cancel each other in the region where they overlap.

$$\begin{aligned}
 I(\mathbf{r}) &= I_0 + \Gamma(\mathbf{r}) + \Gamma^*(\mathbf{r}) \Rightarrow \\
 \widehat{I}(\mathbf{g}) &= I_0\delta(\mathbf{g}) + \widehat{\Gamma}(\mathbf{g}) + \widehat{\Gamma}^*(-\mathbf{g}) \Rightarrow \\
 \widehat{I}(\mathbf{g}) &= I_0\delta(\mathbf{g}) + i\widehat{F}(\mathbf{g})H(\mathbf{g}) + \left[i\widehat{F}(-\mathbf{g})H(-\mathbf{g}) \right]^* \Rightarrow \\
 \widehat{I}(\mathbf{g}) &= I_0\delta(\mathbf{g}) + i\widehat{F}(\mathbf{g})H(\mathbf{g}) - i\widehat{F}^*(-\mathbf{g})H^*(-\mathbf{g}) \Rightarrow \\
 \widehat{I}(\mathbf{g}) &= I_0\delta(\mathbf{g}) + i \left[\widehat{F}(\mathbf{g})H(\mathbf{g}) - \widehat{F}(\mathbf{g})H(-\mathbf{g}) \right] \Rightarrow \\
 \widehat{I}(\mathbf{g}) &= I_0\delta(\mathbf{g}) + i\widehat{F}(\mathbf{g})[H(\mathbf{g}) - H(-\mathbf{g})]
 \end{aligned}$$

Where we used Eq. (1) and two well-know properties of real-valued functions and their Fourier transform:

$$\begin{aligned}
 H^*(\mathbf{g}) &= H(\mathbf{g}) \Rightarrow H^*(-\mathbf{g}) = H(-\mathbf{g}) \\
 F^*(\mathbf{g}) &= F(\mathbf{g}) \Rightarrow \widehat{F}^*(-\mathbf{g}) = \widehat{F}(\mathbf{g})
 \end{aligned}$$

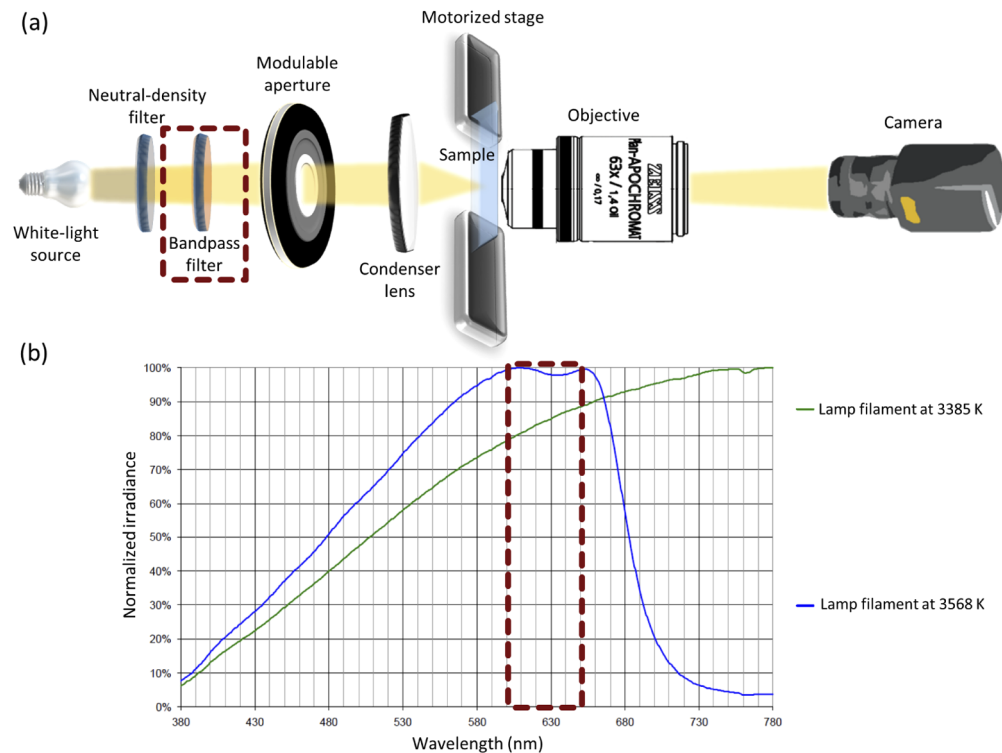


Fig. 2. Adapted transmission microscope. (a) Schematics of the transmission bright-field microscope with a modifiable illumination aperture and two filters to guarantee an illumination regime below saturation (neutral-density filter) and with null dispersion (bandpass filter). (b) Spectrum of the light source. The dashed outline indicates the transmission band of the bandpass filter in (a).

Because of symmetry properties, $H(\mathbf{g}) - H(-\mathbf{g}) = 0$ for all \mathbf{g} such that $H(g_z < 0) \neq 0$. Thus, all the information coming from such \mathbf{g} is filtered out by the optical system and only noise can be contained in such region (the “overlap” region in Fig. 1-b). This fact implies a better high-pass filter than the one proposed previously based on a pure high-pass threshold along the propagation axis [13]. By using the previous relation, we can precisely calculate the support of the transfer function without making use of approximations for the spatial frequency cut-off. With this refined threshold, one can include more spatial frequencies in the phase retrieval process by using the true shape of the transfer function instead of the simple horizontal lower limit $K(g_z)$. In Fig. 1-b, we depict the net gain in the reciprocal space compared to the horizontal-threshold method, and in Fig. 1-c we show that the full support of the transfer function, with the corresponding filtered overlap, can be calculated precisely for several illumination apertures.

In order to use the previous calculations to perform phase retrieval of transparent objects for several illumination apertures, we adapted a standard bright-field transmission microscope with Koehler illumination (Fig. 2-a):

1. We added a modifiable aperture to be able to change the maximum illumination angle at will.

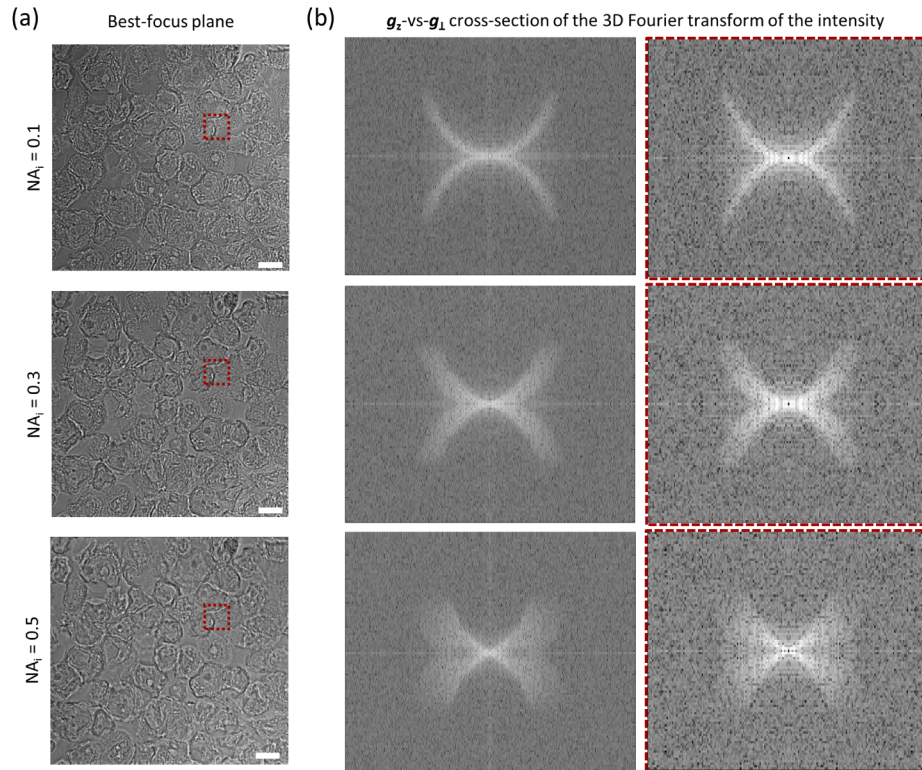


Fig. 3. Spatial frequency content for several illumination apertures. (a) Best-focus slice of the intensity stack of a 5 μm -thick section of fixed human breast cancer cells on a glass slide. Scale bars: 10 μm . (b) Central cross-section of the Fourier transform of the full stack (left column) and of the 100×100 px² region (right column) indicated with the dashed outline in (a). The Fourier transform is plotted as $\log(1 + |I|)$. $NA_d = 1.4$, $\lambda_{i,\min} = 600$ nm, $\lambda_{i,\max} = 650$ nm for all the images.

- We added a neutral-density filter to guarantee the non-saturating regime for all the numerical apertures studied; this element is optional and can be removed if no saturation is encountered with the illumination of interest.
- We added a bandpass filter to guarantee the null-dispersion regime for the samples studied; this element must be adapted to the sample of interest to ensure that its refractive index is independent of the illumination spectrum (no-dispersion condition). The spectrum of the illumination source used in this study is shown in Fig. 2-b along with its relevant range.

We recorded intensity stacks of a 5 μm -thick section of fixed human breast cancer cells for different illumination apertures (Fig. 3-a). We recorded 50 planes spaced by 200 nm from each other along the optical axis, and calculated the 3D Fourier transform of the full-field intensity stack and a sub-region (100 \times 100 px²) of it: the support of the modulation transfer function (within which the information of the sample is contained) is clearly visible (Fig. 3-b) and in accordance with the analytical calculations (Fig. 1-c), along with its dependence on the illumination aperture and its independence of the size of the region. for $\text{NA}_i > 0.5$, the loss in coherence of the illumination light (which result in a decrease of contrast in the cross-spectral density) prevents the scattering from giving enough information about the spatial frequencies contained in the sample.

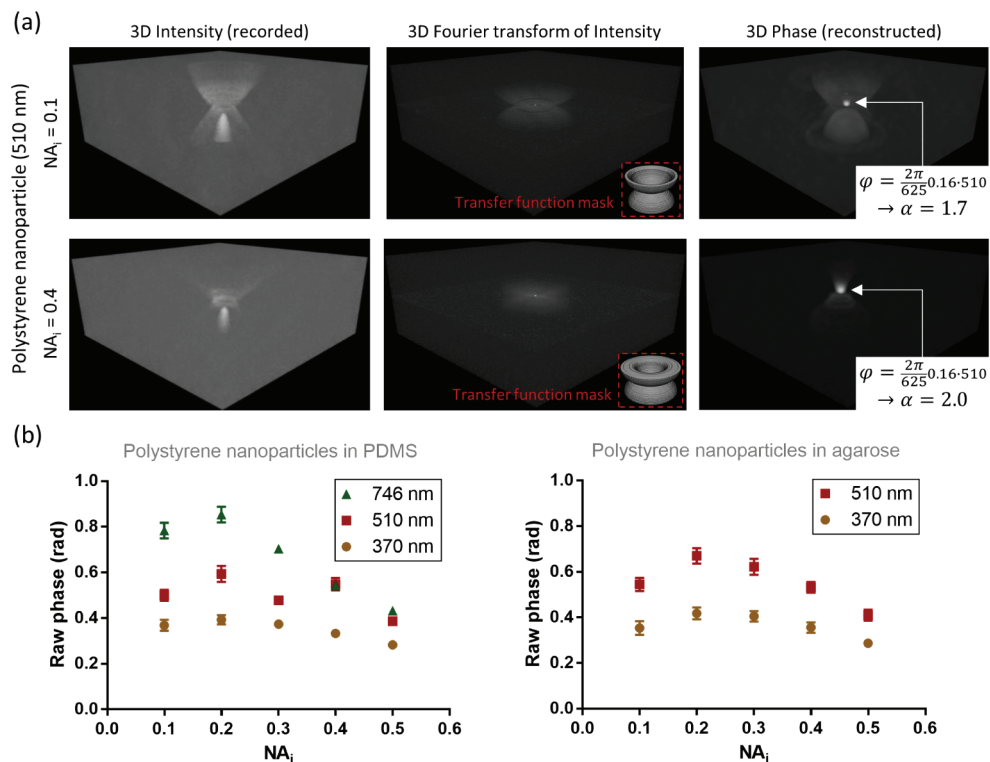


Fig. 4. Phase calibration with polystyrene nanoparticles. (a) Calibration results for a 510 nm polystyrene ($n=1.59$) nanoparticle embedded in agarose gel ($n=1.33$) for different illumination apertures. The central wavelength of the illumination spectrum is 625 nm. (b) Summary of results for the raw phase (*i.e.* Eq. (3) with $\alpha=1$) for different sizes of nanoparticles. Data are plotted as mean \pm s.d. (> 20 nanoparticles per condition)

2.2. Phase calibration for several illumination apertures

In order to measure the dependence of the calibration factor on the illumination aperture, we created samples for which the phase-shift induced on the illumination was known *a priori*. We sparsely embedded polystyrene ($n_{\text{PS}}=1.59$) nanoparticles in agarose ($n=1.33$) and polydimethylsiloxane (PDMS, $n=1.43$) gels to be able to record the interferogram created by individual objects, for which the theoretical phase is known:

$$\varphi = \frac{2\pi}{\lambda_0} (n_{\text{PS}} - n_{\text{gel}}) d \quad (4)$$

where λ_0 is the central wavelength of the illumination spectrum, n_{np} and n_{gel} are the refractive indices of the nanoparticle and the gel, and d is the diameter of the nanoparticle.

In Fig. 4(a), we show some examples of intensity volumes from a particle of 510 nm. The cone of the scattered light is clearly visible and depends on the angle with which the illumination encounters the scatterer. For smaller angles (lower NA_i), the scattered light contributes more to the interferogram, as anticipated based on the spatial coherence of the illumination [13]. We then calculated the Fourier transform of the intensity stack. Finally, we applied the transfer function mask and an inverse Fourier transformation to obtain the phase induced by the nanoparticle:

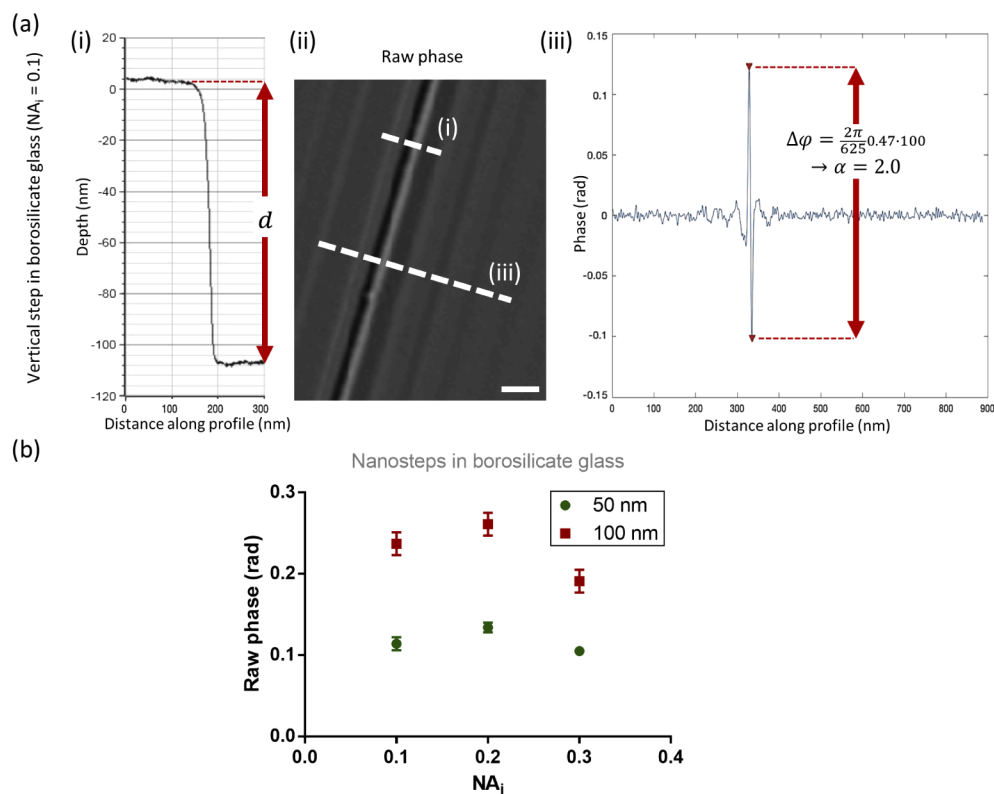


Fig. 5. Phase calibration with nanosteps in a borosilicate glass substrate. (a) Calibration results for a 100 nm-high step of borosilicate glass ($n=1.47$): (i) topographic profile of the cross-section of the edge; (ii) top view of the step showed as the maximum projection of the raw phase (scale bar: 150 nm); (iii) raw phase profile perpendicularly to the edge. (b) Summary of results for the raw phase for different step depths. Data are plotted as mean \pm s.d. (>10 edges per condition).

we see how the 3D phase is much closer to the shape of a particle than is its corresponding 3D intensity. In Fig. 4(b), we show the raw reconstructed phase for polystyrene nanoparticles of several sizes: we observe that for higher NA_i (*i.e.* less spatial coherence of the illumination), the phase for large objects tends to decrease, as anticipated in other work [13]. This phenomenon is more pronounced for larger nanoparticles, since they locally scatter less than smaller ones. For this reason, we excluded the largest nanoparticles (746 nm) in the calibration of the largest NA_i (0.4 and 0.5). For all the other conditions, we calculated the corresponding calibration factor by matching the maximum of the reconstructed phase with the theoretical phase shift given by Eq. (4).

In order to get access to smaller phase shifts, we fabricated holes of 50 and 100 nm depth in borosilicate glass ($n_{BS}=1.47$) and performed the same analysis. We measured the physical height of the edges of the structures (Fig. 5(a)-i), applied the image-processing algorithm to retrieve the phase shift (Fig. 5(a)-ii) and calculated the calibration factor by matching with $\varphi = \frac{2\pi}{\lambda_0} n_{BS} h$ (Fig. 5(a)-iii), with h the depth of the nanostep. Because of the sharp vertical edge, illumination from too large angles ($NA_i=0.4$ and 0.5) can undergo total internal reflection and generate artifacts that bias the reconstruction algorithm, and are thus excluded from the calibration. The results for the raw phase for the other illumination apertures are shown in Fig. 5(b).

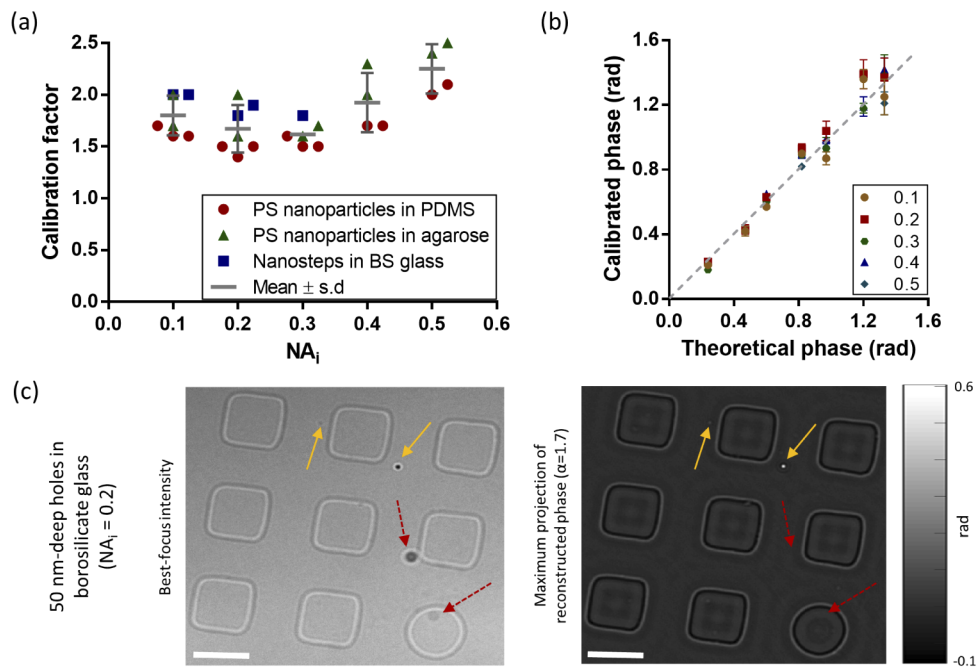


Fig. 6. Calibration summary. (a) Calibration factor as a function of the illumination numerical aperture for all the conditions tested. (b) Calibrated reconstructed phase versus theoretical phase for several illumination apertures. Data are plotted as mean \pm s.d. (>20 points per condition). The dashed line indicates the perfect matching. (c) Calibration results for square and circular holes in borosilicate glass. Solid yellow arrows indicate diffractive particles on the sample: their phase is retrieved during the processing of the 3D Intensity. Dashed red arrows indicate image artefacts due to dusts/defects on the optical parts and on the camera sensor: their presence do not affect the retrieved phase, since they appear as constant in the 3D intensity and, thus, are filtered out by the transfer function mask. Scale bars: 10 μm .

We show all the calibration factors for all the samples and illumination apertures measured in Fig. 6(a). We observe a slight decrease from $NA_i=0.1$ to 0.3, and a more accentuated increase for $NA_i=0.4$ and 0.5. However, by using the average value for each NA_i , the reconstructed phase is very close to the corresponding theoretical phase (Fig. 6(b)) and is able to give the phase-shift of microstructures of small depth (Fig. 6(c)).

2.3. Dependence of the 3D reconstruction of a complex nanostructured sample on the illumination aperture

Using the thus obtained calibration factors, we then studied the behavior of the reconstructed 3D phase of a complex nanostructured sample (i.e. containing many different spatial frequencies in every direction) upon varying the illumination aperture. We used a 5 μm -thick layer of fixed human breast cancer cells, the structure of which is complex enough to fill the entire support of the transfer function of the optical system (as shown in Fig. 3(b)). We analyzed the voxel-by-voxel correlation of the entire reconstructed volume for each NA_i with each other NA_i (Fig. 7(a)). As expected, we observe that close NA_i s result in more similar values for the same voxel (higher correlation) than do farther NA_i s (lower correlation). Moreover, we observe that some scattering structures (such as the nucleolus of the cell) are reconstructed better when using a lower NA_i (Fig. 7(b)), as predictable when considering the higher spatial correlation for such illumination conditions also reported in previous work [13]. Finally, we analyzed the distribution of the phase values along the optical axis for several NA_i s (Fig. 8). First, we observe that the values for lower NA_i span a larger range for every section along the optical axis. Second, we notice that the interquartile range of the distributions is larger for sections that are in the middle of the recorded volume, which is in accordance with the presence of the sample at this location: the 5 μm -layer of cells (≈ 25 planes) lies between section 3 and 8.

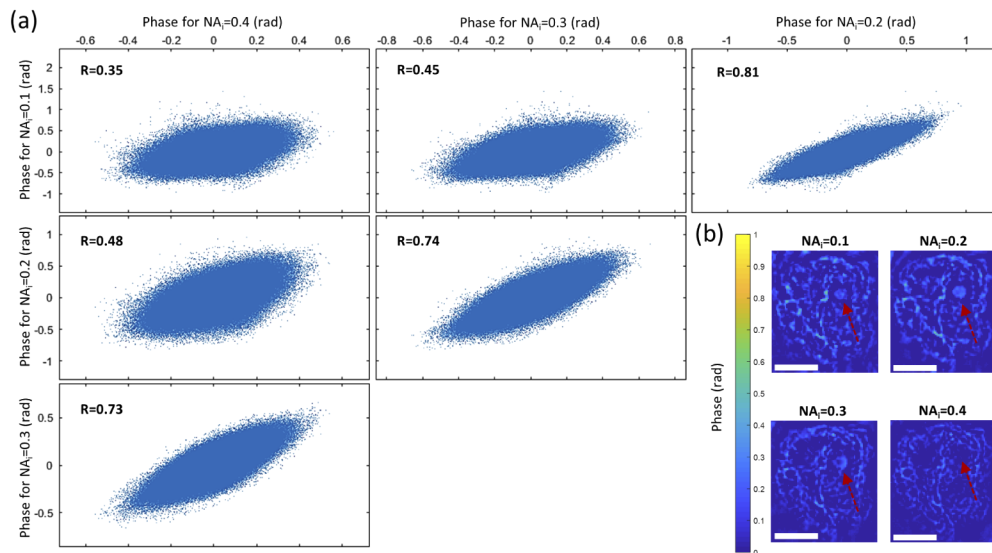


Fig. 7. Influence of the illumination aperture on the phase retrieval of a complex 3D nanostructured sample. (a) Pairwise voxel-by-voxel correlation of the 3D phase of a 5 μm -thick/50 μm -large/50 μm -wide layer of human breast cancer cells for illumination numerical apertures from 0.1 to 0.4. The Pearson correlation coefficient for each pair is indicated in the corresponding graph. (b) Color-coded phase of the middle plane of a human breast cancer cell for NA_i s from 0.1 to 0.4. The dashed arrows indicate the nucleolus of the cell. Scale bar: 5 μm .

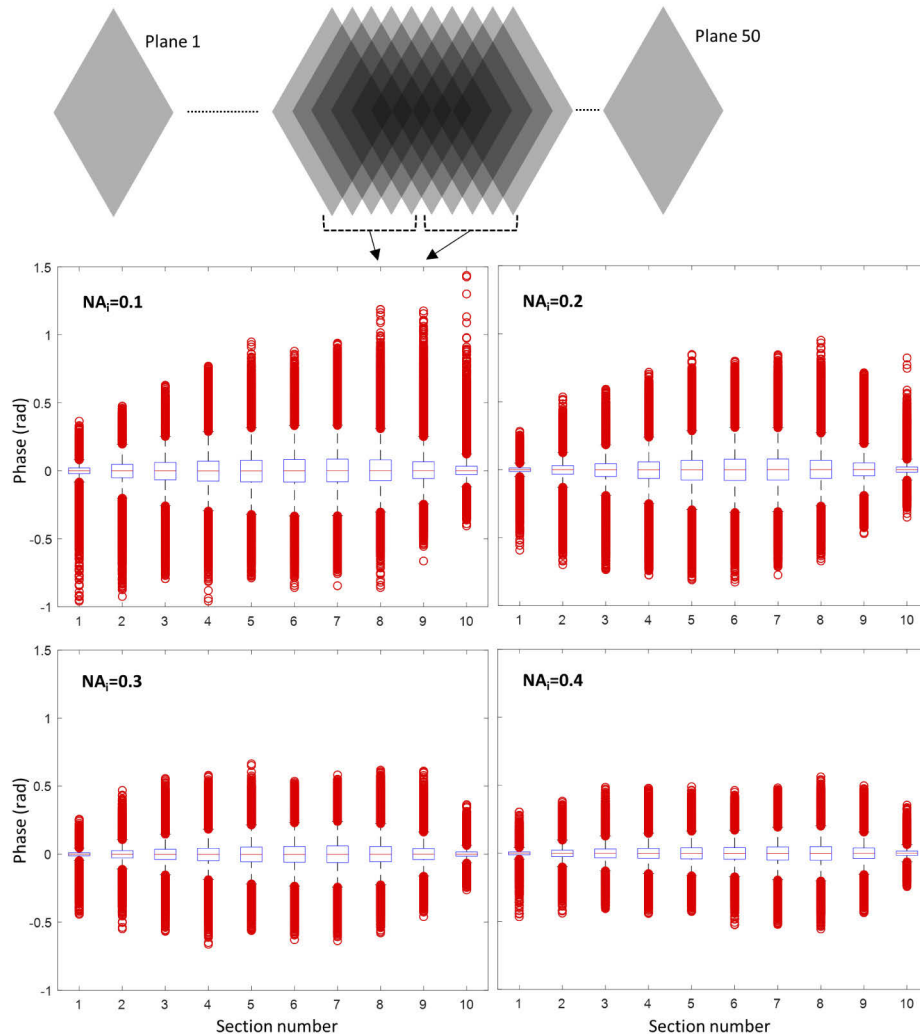


Fig. 8. Dependence of the variation of the phase along the optical axis upon the illumination aperture. Tukey boxplots of the values of the phase of a 5 μm -thick/50 μm -large/50 μm -wide layer of human breast cancer cells for NA_i s from 0.1 to 0.4. Each boxplot displays the distribution of the phase for a set of 5 of the 50 planes recorded along the optical axis (inter-plane distance=200 nm) over the full area of the sample.

3. Discussion

In this work, we built upon previous approaches for quantitative phase retrieval in order to expand the potential of a standard transmission microscope to collect information on the spatial frequencies of transparent samples by modulating the illumination numerical aperture. We first showed that the overlap region of the modulation transfer function and its conjugate cancels out independently of the illumination aperture because of symmetry properties. This feature enabled us to give a precise shape to the transfer function mask in the Fourier space for several illumination apertures, which we applied to calibration samples such as nanoparticles embedded in gels and microfabricated nanosteps in a glass substrate. We then concluded by comparing the quantitative phase of a complex 3D sample when reconstructed by using different illumination apertures.

Regarding the dependence of the modulation transfer function on the illumination numerical aperture, Fig. 1(c) shows how the support of the transfer function changes its shape and the overlap region increases when increasing the illumination aperture, as also suggested previously [13]. However, depending on the spatial frequencies present in the sample, it is not always suitable to increase the illumination aperture, since some spatial frequency regions may be excluded depending on the illumination spectrum and the detection aperture. One should thus adjust the microscope specifications (illumination spectrum and aperture, and detection objective) to the sample of interest in order to obtain the most relevant information on its spatial frequency content. Moreover, increasing the illumination aperture decreases the spatial coherence, which is key to create an informative interferogram of the sample [13,17], and for $NA_i > 0.5$, the loss in coherence of the illumination light (which results in a decrease of contrast in the cross-spectral density) prevents the scattering from giving enough information about the spatial frequencies contained in the sample. This behavior could be mitigated by using annular illumination instead of circular illumination [8,17], however, the transfer function and the retrieval algorithm must be adjusted accordingly. In this regard, we observe that the spatial frequency content collected in our experimental conditions with circular illumination (Fig. 3(b)) follow the theoretical prediction in the full range of illumination apertures tested. The smoothness of the cross-section of the sub-region is lower than for the full-field image simply because the spatial frequency unit is calculated based on the size of the image, which is obviously larger for the full-field stack and thus results in an apparent finer pixelization. We highlight this independence of transfer function support from the size of the image because the speed of the reconstruction algorithm highly decreases with the size of the stack to process. Therefore, in cases where faster results are desired, using a sub-region which only includes the objects of interest does guarantee the same quality of results.

The elongated shape of the reconstructed particles (Fig. 4(a)) is the result of the missing-cone problem typical of some phase microscopy methods [2,19,20], which is reflected, in our reconstruction algorithm, in the low-frequency overlap we mentioned in section 2.1, which contains no information on this spatial frequency range. This effect is clearly more visible for larger NA_i (Fig. 4(a)) because the overlap expands when increasing the illumination aperture (Fig. 1(c)).

Interestingly, the majority of the factors resulting from phase calibration lay within the range 1.5-2.0 (Fig. 6(a)) except for the ones obtained for the largest illumination aperture $NA_i=0.5$ and partially for $NA_i=0.4$. This is a quantitative consequence of the decreased spatial coherence of the illumination for such large apertures, which results in an artificial increase of the calibration factor to compensate for the physical decrease of the raw phase that is obtainable from the interferogram (Fig. 4(b)). Despite this behavior, we observe that the calibrated phase match the theoretical one very closely (Fig. 6(b)). Another interesting conclusion from Fig. 6(b) is that this method is more consistent for the retrieval of small phase-shifts, which is coherent with the shape of the modulation transfer function, the wings of which “expands” when increasing the distance

from the origin (*i.e.* towards higher spatial frequencies). For a similar filtering phenomenon (*i.e.* the exclusion of the low spatial frequency included in the overlap, Fig. 1(b)), the image artifacts due to defects in the optical elements or on the camera sensor are not kept in the phase image and result in a null phase shift (dashed arrows in Fig. 6(c)). Moreover, the difference in the calibration factor found for $NA_i=0.26$ in previous work [13] seems to corroborate the hypothesis that the calibration step is required because of specific spatial filtering properties of the specific optical system.

Moreover, the correlation between close values of NA_i s (Fig. 7(a)) indicates that the reconstructed phase of each voxel varies continuously with respect to the NA_i , which guarantee robustness. Finally, based on the observation on both calibration samples (Fig. 4(a)) and complex 3D nanostructured samples (Fig. 7(b) and 8), it seems that the decreased spatial coherence for larger illumination apertures is detrimental for the retrieval of the phase of nanostructures. This suggests that the best range for nanostructure phase retrieval for this method lies between $NA_i=0.1$ and $NA_i=0.3$.

Compared to previous approaches relying on paraxial approximations [8–11] or on deconvolution algorithms with empirical terms for regularization [6,14], we showed that it is possible to reliably calibrate the optical system for a large range of illumination apertures with the use of a specific calibration factor to retrieve the quantitative phase of transparent objects. Compared to other methods employing differential phase contrast through sequential spatial illumination with patterned LED arrays and refractive index retrieval with regularization algorithms [2], the present procedure only requires standard diaphragms, which can simplify the experimental setup and the recording procedure. Moreover, the empirical adjustment of the calibration factor also mitigates the missing-cone problem for which regularization a regularization algorithm is necessary for retrieval correction. However, the possibilities introduced by a patterned LED array illumination can be more advantageous when willing to push the limit of resolution, because of the customizability of the illumination which can offer spatial frequency coverages beyond the ones available with circular illumination (such as the annular illumination mentioned above to even more specific illumination patterns).

With the current work, we also complement previous simulation results on the impact of the illumination properties on the retrieval of the 3-dimensional phase with conventional wide-field microscopes [18]. Further investigation may address the introduction of a correction term for absorptive samples, and assess a method to combine the full information obtained from all the numerical apertures at once.

In conclusion, because of the simplicity of the method and the properties that we showed in this work, we believe that our assessment of the phase calibration of a transmission microscope for several illumination apertures will be of support to the researchers and the engineers willing to measure the 3-dimensional structure of transparent objects at the nanoscale.

4. Methods

4.1. Sample preparation

The polystyrene nanospheres were purchased from Polysciences: Polybead Microspheres series with diameters of 350 nm (#035956), 500 nm (#050956) and 750 nm (#075956). PDMS prepolymer and curing agent were from Dow Corning (Sylgard 184 Silicon Elastomer). 200 μ l of diluted solution of nanospheres were let dry in a petri-dish and subsequently covered with a solution 10:1 of PDMS prepolymer:curing agent to make a thin membrane of few mm thickness. The PDMS was cured for 1 h at 80°C and then peeled off from the petri-dish. Alternatively, the solution with the nanospheres was directly mixed with a 2% agarose solution with a 1:1 ratio and let gelify at 4% for 2 min. For the glass step samples, we performed the following fabrication procedure: a borofloat-33 wafer (100 nm diameter, 500 μ m thickness) was cleaned with Piranha solution and then backside-coated with a 150 nm-thick layer of Titanium; the wafer

was then cleaned by using an oxygen plasma (7 min at 0.5 mbar and 200 W) and treated with hexamethyldisilazane (HMDS) vapor (125°C, 3-8 mmHg, exposure time 10 s). Then, 600 nm of AZ ECI 3000 photoresist was deposited on top of it and baked at 100°C for 90 s. Photolithography was performed by direct writing with a 405 nm laser at 120 mJ/cm² followed by development at 110°C for 60 s. Dry etching was then performed by using a He-CHF₃ plasma (etching rate of 200 nm/min and selectivity 1.7:1). The remaining photoresist was removed with a plasma oxygen (7 min at 0.5 mbar and 200 W). Finally, the backside Titanium layer was removed by ion beam etching. Glass slides with cells were purchased from AMS Biotechnology (Europe) Ltd – Switzerland. They were deparaffinized in 3 HistoClear II solutions (National Diagnostics, USA) for 5 minutes each. Then, they were transferred to gradual ethanol series of 100%, 100%, 95%, 70%, 40%, for 2 minutes each. Finally, the slide was mounted with SlowFade Gold Antifade mounting medium (Life Technologies, USA), and a coverslip (Menzel-Glaser, 170 μm thickness) was put on top of it.

4.2. Optical imaging

For the imaging, we used the commercial UPRIGHT Zeiss AxioImager M1, equipped with the 12 V/100 W halogen lamp for the illumination. The bandpass and the neutral density filters were purchased from Edmund Optics (product numbers #86-965 and #62-671 respectively). The condenser lens had a NA=0.9. The objective used was a Plan-Apochromat 63×/NA=1.4 oil-immersion objective with a working distance of 0.19 mm from Zeiss. The camera was an Axiocam MRm (B/W) with a resolution of 1388×1040 and a detector size of 6.45×6.45 μm². Each sample was imaged by recording a *z*-stack of the full field-of-view (exposure time between 1 and 10 ms).

4.3. Image processing and data analysis

Images were saved as TIFF files and processed for phase retrieval with a custom modified version of a public algorithm [21] written with MATLAB2018b [22]. Briefly, the bright-field stack is opened and a square window is selected. Subsequently, the stack is mirrored on the *z* and *x* axes and Fourier-transformed. The modulation transfer function mask is then applied prior to an inverse Fourier transformation. Finally, the 3D phase is retrieved by using Eq. (3). The correlation and the axial sectioning analysis were performed by using custom made MATLAB scripts. For the correlation analysis, the 3D data of the resulting phase stacks were transformed in 1D vectors associated to the corresponding NA_{*j*}. Subsequently, the pairwise voxel-by-voxel correlations between different NA_{*j*}s were performed. For the axial sectioning analysis, the stacks were partitioned into 10 adjacent sections, and the distribution of each of them was displayed as a Tukey boxplot.

Disclosures

The authors declare no conflicts of interest.

References

1. W. J. Choi, D. I. Jeon, S.-G. Ahn, J.-H. Yoon, S. Kim, and B. H. Lee, "Full-field optical coherence microscopy for identifying live cancer cells by quantitative measurement of refractive index distribution," *Opt. Express* **18**(22), 23285–23295 (2010).
2. M. Chen, L. Tian, and L. Waller, "3D differential phase contrast microscopy," *Biomed. Opt. Express* **7**(10), 3940–3950 (2016).
3. W. Choi, C. Fang-Yen, K. Badizadegan, S. Oh, N. Lue, R. R. Dasari, and M. S. Feld, "Tomographic phase microscopy," *Nat. Methods* **4**(9), 717–719 (2007).
4. Y. Park, M. Diez-Silva, G. Popescu, G. Lykotrafitis, W. Choi, M. S. Feld, and S. Suresh, "Refractive index maps and membrane dynamics of human red blood cells parasitized by *Plasmodium falciparum*," *Proc. Natl. Acad. Sci.* **105**(37), 13730–13735 (2008).

5. Y. Cotte, F. Toy, P. Jourdain, N. Pavillon, D. Boss, P. Magistretti, P. Marquet, and C. Depeursinge, "Marker-free phase nanoscopy," *Nat. Photonics* **7**(2), 113–117 (2013).
6. T. Kim, R. Zhou, M. Mir, S. D. Babacan, P. S. Carney, L. L. Goddard, and G. Popescu, "White-light diffraction tomography of unlabelled live cells," *Nat. Photonics* **8**(3), 256–263 (2014).
7. S. S. Kou, L. Waller, G. Barbastathis, and C. J. R. Sheppard, "Transport-of-intensity approach to differential interference contrast (TI-DIC) microscopy for quantitative phase imaging," *Opt. Lett.* **35**(3), 447–449 (2010).
8. C. Zuo, J. Sun, J. Li, J. Zhang, A. Asundi, and Q. Chen, "High-resolution transport-of-intensity quantitative phase microscopy with annular illumination," *Sci. Rep.* **7**(1), 7654 (2017).
9. M. R. Teague, "Deterministic phase retrieval: a Green's function solution," *J. Opt. Soc. Am.* **73**(11), 1434–1441 (1983).
10. N. Streibl, "Phase imaging by the transport equation of intensity," *Opt. Commun.* **49**(1), 6–10 (1984).
11. C. J. R. Sheppard, "Three-dimensional phase imaging with the intensity transport equation," *Appl. Opt.* **41**(28), 5951–5955 (2002).
12. E. Wolf, "Three-dimensional structure determination of semi-transparent objects from holographic data," *Opt. Commun.* **1**(4), 153–156 (1969).
13. A. Descoux, K. S. Grusmayer, E. Bostan, T. Lukes, A. Bouwens, A. Sharipov, S. Geissbuehler, A.-L. Mahul-Mellier, H. A. Lashuel, M. Leutenegger, and T. Lasser, "Combined multi-plane phase retrieval and super-resolution optical fluctuation imaging for 4D cell microscopy," *Nat. Photonics* **12**(3), 165–172 (2018).
14. J. M. Soto, J. A. Rodrigo, and T. Alieva, "Label-free quantitative 3D tomographic imaging for partially coherent light microscopy," *Opt. Express* **25**(14), 15699–15712 (2017).
15. Z. Jingshan, R. A. Claus, J. Dauwels, L. Tian, and L. Waller, "Transport of Intensity phase imaging by intensity spectrum fitting of exponentially spaced defocus planes," *Opt. Express* **22**(9), 10661–10674 (2014).
16. L. Tian and L. Waller, "Quantitative differential phase contrast imaging in an LED array microscope," *Opt. Express* **23**(9), 11394–11403 (2015).
17. J. Li, Q. Chen, J. Sun, J. Zhang, J. Ding, and C. Zuo, "Three-dimensional tomographic microscopy technique with multi-frequency combination with partially coherent illuminations," *Biomed. Opt. Express* **9**(6), 2526–2542 (2018).
18. J. A. Rodrigo, J. M. Soto, and T. Alieva, "Fast label-free optical diffraction tomography compatible with conventional wide-field microscopes," *Opt. Express* **11060**, 1106016 (2010).
19. J. Lim, K. Lee, K. H. Jin, S. Shin, S. Lee, Y. Park, and J. C. Ye, "Comparative study of iterative reconstruction algorithms for missing cone problems in optical diffraction tomography," *Opt. Express* **23**(13), 16933–16948 (2015).
20. C. J. R. Sheppard, M. Gu, Y. Kawata, and S. Kawata, "Three-dimensional transfer functions for high-aperture systems," *J. Opt. Soc. Am. A* **11**(2), 593–598 (1994).
21. "TomographicPhaseRetrieval - <https://c4science.ch/source/TomPhaseRet/> - 17/2/2020,".
22. MATLAB, "Version R2018a," (2018).